

LES RESULTS OF THE GASS-EUCLIPSE LAGRANGIAN STRATOCUMULUS TO SHALLOW CUMULUS TRANSITION CASES

S. R. de ROODE¹, *I. SANDU^{2,3}, J. J. VAN DER DUSSEN¹, A. S. ACKERMAN⁴,
P. N. BLOSSEY⁵, A. LOCK⁶, A. P. SIEBESMA¹, and B. STEVENS³

¹*Delft University of Technology, The Netherlands*

²*ECMWF, Reading, UK*

³*Max-Planck Institut für Meteorologie, Hamburg, Germany*

⁴*NASA GISS, New York, NY, USA*

⁵*University of Washington, Seattle, WA, USA*

⁶*UK Meteorological Office, Exeter, UK*

⁷*KNMI, De Bilt, The Netherlands*

ABSTRACT

As part of the European Union Cloud Intercomparison, Process Study & Evaluation Project (EUCLIPSE) project five LES models were used to simulate four different Global Atmospheric System Studies (GASS) model intercomparison cases of a Lagrangian stratocumulus to shallow cumulus transition. For each case the models show a gradual increase in the boundary layer depth. The stratocumulus cloud layer also rises with time, whereas the temporal change in cumulus cloud base height is rather modest. The degree of decoupling, as quantified by the difference in the mean subcloud and cloud layer total specific humidity and liquid water potential temperature is compared to results from aircraft observations as reported by Wood and Bretherton (2004). Like the observations, the LES results exhibit a larger difference for deeper boundary layers, although the differences are somewhat larger in the LES fields. The dynamics in the decoupled subcloud layer are found to be similar to the dry convective boundary layer. A clear diurnal cycle in the shallow cumulus moisture transport is found. During the day moisture builds up in the subcloud layer, which is being redistributed by the cumuli towards the stratocumulus layer above during the night. Overall, the mean humidity transport at the top of the subcloud layer is only slightly smaller than the surface evaporation, thus being close to a zero-flux divergence. Last, it is found that during the night the boundary layer is close to a quasi-steady state.

1. INTRODUCTION

The presence of a strong thermal inversion in the subtropical part of the Hadley circulation efficiently traps the moisture that is evaporated from the ocean. As a result extended stratocumulus cloud fields persist in these areas. This cloudy air is transported equatorwards over increasingly higher sea surface temperatures by the trade-winds, and stratocumulus is gradually replaced by shallow cumulus. The latter cloud type has a lower cloud fraction, allowing a much higher fraction of the downwelling

* Corresponding author address: Stephan de Roode, Geoscience and Remote Sensing, Delft University of Technology, Delft, The Netherlands (s.r.deroode@tudelft.nl)

shortwave radiation to reach the sea surface. It is therefore important for weather and climate models to realistically represent this cloud regime.

To investigate the ability of both single-column model (SCM) versions of global weather and climate models and large-eddy simulation (LES) models to reproduce the transition between marine stratocumulus and shallow cumulus four Lagrangian cases are proposed for an intercomparison study of both SCM and LES within the EUCLIPSE-GASS framework. The first case is a revisited model intercomparison case based on the Atlantic Stratocumulus to Cumulus Transition Experiment (ASTEX) field campaign (Albrecht et al., 1995; Bretherton and Pincus, 1995; Bretherton et al., 1995; De Roode and Duykerke, 1997), which already served in the past for an intercomparison of SCMs (Bretherton et al., 1999). The increase in computational power allows us now to perform 3-D Large Eddy Simulations of this case as well. The second case gathers in fact a set of three composite transitions, based on the observational study of the transitions in boundary layer cloudiness described in Sandu et al. (2010) and Sandu and Stevens (2011). While ASTEX offers the opportunity to evaluate models against in situ data, this set of composite transitions represents a more idealized framework for model evaluation, which offers the possibility of comparing the models for a variety of transition cases, which differ for example in terms of amplitude or timescale of the transition.

2. DESCRIPTION OF THE INTERCOMPARISON CASES

2.1 Large-scale and initial conditions

The ASTEX case is based on five subsequent sets of aircraft observations collected during a two-day period over the Atlantic Ocean. It differs from the SCM intercomparison case originally proposed by (Bretherton et al., 1999) as its initial state is based on the second flight A209 of the ASTEX Lagrangian and identical to a previous GCSS LES model intercomparison case led by Peter Duykerke in 1995. However, due to the limited computational resources at that time, the simulations lasted three hours only and used a simple parameterization for the longwave

radiative cooling at the top of the cloud layer and lacked precipitation.

Sandu and Stevens (2011) present the setup of the Reference case, which is based on a composite of the large-scale conditions encountered along a set of individual trajectories performed for the northeastern Pacific during the summer months of 2006 and 2007. Both the initial profiles and the large-scale conditions represent the medians of the distributions of these various properties obtained from the European Centre for Medium-Range Weather Forecasts (ECMWF) Interim Re-Analysis (ERA-Interim) for the analyzed set of trajectories. For the study presented in this paper an additional 'Slow' and 'Fast' composite case are proposed, each of which has a slightly different initial thermodynamic state.

The initial vertical profiles of the liquid water potential temperature (θ_L) and total water specific humidity (q_T) for the four different stratocumulus to shallow cumulus experiments are shown in Figure 1. The ASTEX case has the smallest value for the initial inversion jump in the liquid water potential temperature, which gradually increases in magnitude for the Fast, Reference and Slow cases, respectively. The inversion jumps in the total specific humidities are also different for each case, with the Slow case having the driest free atmosphere. The input files provided on the EUCLIPSE website (<http://www.euclipse.nl>) provide the vertical profiles up to the stratosphere, including the one for ozone.

Figure 2 shows that the sea surface temperature (SST) increases with time for each case, which reflects the lagrangian equatorwards advection of the simulated airmass. The LES models compute the sensible and latent heat fluxes with aid of Monin-Obukhov similarity theory and the prescribed SST.

For the ASTEX case the large-scale divergence gradually decreases with time, whereas a weakening of the wind velocities is taken into account by a time-varying geostrophic forcing. For the composite cases both the large-scale divergence and geostrophic forcing are constant in time. Because the lower tropospheric stability is key for the evolution of the SCT, a realistic tendency of the temperature is needed in particular as the simulations were performed for a period of two or three days. Therefore, for a faithful representation of the radiative transfer in a cloudy atmosphere all models applied a full radiation code. The simulations lasted 72 hours, except for ASTEX which was simulated for 40 hours.

2.2 Participating LES models and numerical set-up

Table 1 lists the models and their acronyms, along with contributors from each participating group, as well as the main references to the models. The vertical grid resolution in the lower 540 m is $\Delta z = 15$ m. To represent the sharp inversion layer capping the cloudy boundary layer the resolution is gradually refined above this height, and between 645 and 2400 m $\Delta z = 5$ m. The horizontal domain size is 4.48×4.48 km² and the number of grid points in the horizontal directions is $N_x = N_y = 128$, implying a horizontal resolution $\Delta x = \Delta y = 35$ m.

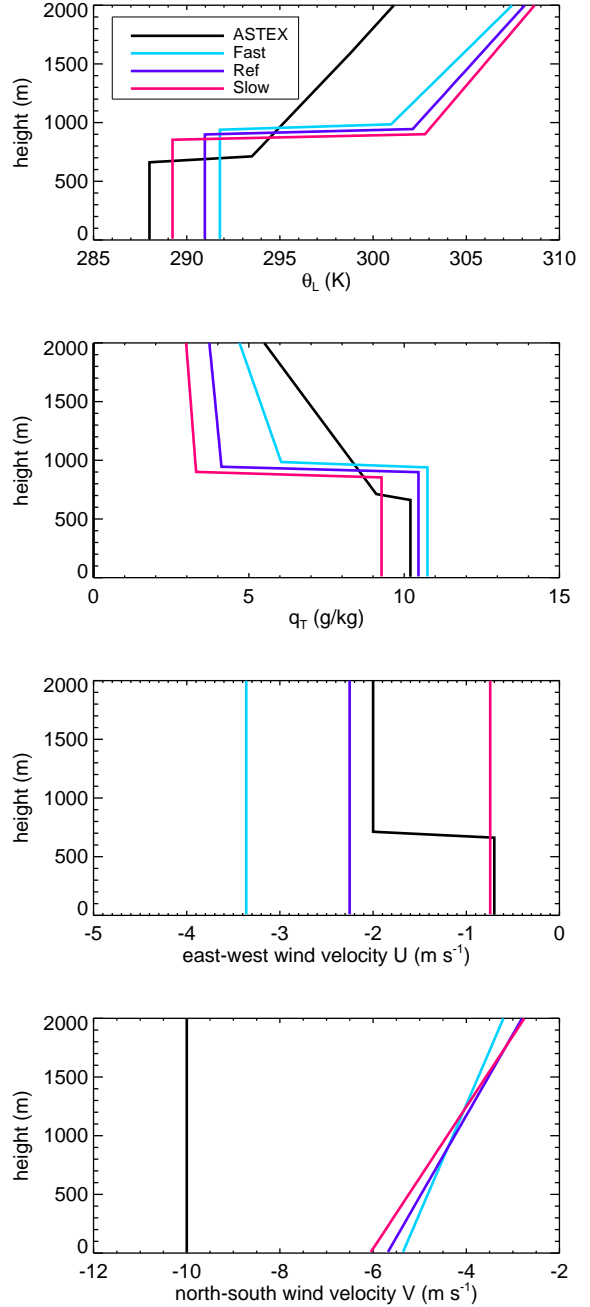


FIG. 1: Vertical profiles of the initial liquid water potential temperature θ_L , total water content q_T , and the horizontal wind velocity components U and V for the ASTEX, Fast, Reference and Slow cases. The line styles are according to the legend.

LES model	Institution	References	Participants
DALES	TU Delft	Heus et al. (2010)	Stephan de Roode and Johan van der Dussen
MPI/UCLA	MPI-Hamburg	Stevens et al. (2005)	Irina Sandu and Bjorn Stevens
SAM	U. Washington	Khairoutdinov and Randall (2005)	Peter Blossey
MOLEM	UKMO	Lock (2009)	Adrian Lock
DHARMA	NASA Langley Research Center	Stevens et al. (2002)	Andy Ackerman

Table 1: Participating models and contributors.

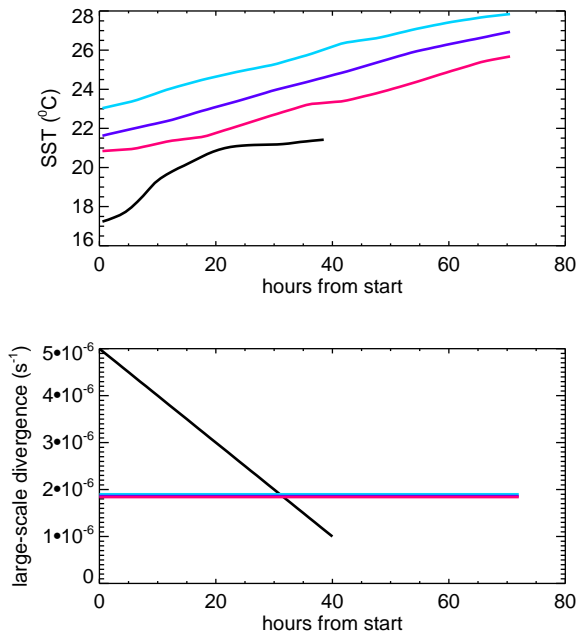


FIG. 2: Prescribed sea surface temperature and large-scale divergence as a function of time for the four stratocumulus to shallow cumulus transition cases. The line styles are the same as in Figure 1.

3. RESULTS

3.1 Mean state

Figure 3 shows the cloud boundaries that were diagnosed from the hourly-mean cloud fraction c_f . The cumulus cloud base $z_{cu,base}$ is defined as the lowest height where $c_f > 0.005$. Likewise, the stratocumulus cloud base height $z_{sc,base}$ is defined as the lowest height where $c_f > 0.9$, and the same criterion is applied to find the stratocumulus cloud top height $z_{sc,top}$. No stratocumulus data are plotted in the figures at times when these criteria are not satisfied. During the last 24 hours of the simulations of all cases the cumulus cloud base height appears to reach a steady state, with $z_{cu,base}$ slightly below 1 km for the composite cases.

The evolution of the subcloud mixed layer height z_{ML} can be well explained from its budget equation (Neggers et al., 2006)

$$\frac{\partial z_{ML}}{\partial t} = E + \bar{w} - M, \quad (1)$$

where E is top entrainment velocity, \bar{w} is the large-scale vertical velocity at z_{ML} and $M > 0$ is the shallow cumulus mass flux at z_{ML} . The term $E > 0$ represents the process of air being mixed into the subcloud layer from above. The cumulus mass flux M acts as a sink term in the mixed-layer mass budget. In the cases considered here the subsidence rate $\bar{w} < 0$. In summary, a steady-state mixed-layer subcloud height implies a balance between entrainment growth and a decrease due to cumulus mass flux and subsidence.

This evolution of the cumulus cloud base height is in striking contrast with the evolution of the stratocumulus cloud layer, which top exhibits a continuous growth. The rate of stratocumulus cloud top rise is well correlated with the temperature jump across the inversion, where a smaller value allows for more entrainment. The LES models show a remarkable good agreement in both the cumulus cloud base and stratocumulus cloud top heights. However, the stratocumulus cloud base height exhibits some more intermodel spread.

Figure 4 shows that after some hours from sunset the stratocumulus cloud layer can become sufficiently thin leaving columns of clear air. However, well before sunset the stratocumulus cloud deck can recuperate. The LES models are rather well consistent in predicting the break up and recovery of the stratocumulus, although the tim-

ing and cloud cover vary significantly. The LES models agree well in the diurnal of the cloud liquid water path (LWP), although the amplitude is larger in the MPI/UCLA and DHARMA models. In the next section attention will be paid to the precipitation rates at the stratocumulus cloud base.

Figure 6 shows vertical profiles of θ_L and q_T for the 50th hour of the Reference case. The cloud layer is warmer and drier than the subcloud layer, both of which are vertically well mixed. The LES results resemble a decoupled boundary layer structure as is assumed in the conceptual model by Park et al. (2004). They defined decoupling parameters α_θ and α_q , respectively,

$$\alpha_\theta = \frac{\theta_L(z_i^-) - \theta_{L,ML}}{\theta_L(z_i^+) - \theta_{L,ML}}, \quad (2)$$

$$\alpha_q = \frac{q_T(z_i^-) - q_{T,ML}}{q_T(z_i^+) - q_{T,ML}}, \quad (3)$$

where z_i^+ and z_i^- are the heights just above and below the inversion layer. The cloudy boundary layer is perfectly well mixed if the decoupling parameter is equal to zero. To evaluate the decoupling parameter from the LES results, we calculated the mixed layer value between the surface and cumulus cloud base height. Stratocumulus cloud-top values were obtained by calculating the mean value between its cloud base and top heights. Figure 7 shows the decoupling parameters α_q and α_θ for the cases where stratocumulus have a cloud fraction larger than 0.9. The figure also shows a fit of α_q that was made on the basis of results from aircraft observations presented in the Figure 5 by Wood and Bretherton (2004), where it should be noted that this study took did not use a stratocumulus cloud fraction criterion. The LES modeling results give $\alpha_q > \alpha_\theta$. This was also found by Wood and Bretherton (2004), although the results presented in their Table 2 appear to give a somewhat smaller difference than the LES results. The question whether thin and broken stratocumulus at the top of the boundary layer in the LES models have a different degree of decoupling needs to be explored further.

4. SUBCLOUD LAYER TURBULENCE STRUCTURE

The fact that the decoupling parameters are nonzero warrants investigation of the subcloud layer dynamics. In particular, De Roode and Duykerke (1997) questioned whether the vertical velocity variance $\langle w'^2 \rangle$ in a decoupled subcloud layer can be predicted by the free convective similarity relation proposed by Lenschow et al. (1980)

$$\frac{\langle w'^2 \rangle}{w_*^2} = 1.8 \left(\frac{z}{z_{ML}} \right)^{2/3} \left(1 - 0.8 \frac{z}{z_{ML}} \right)^2, \quad (4)$$

with z_{ML} the depth of the subcloud mixed layer which we here define by the height of the minimum value of the buoyancy flux. The convective velocity scale is defined by

$$w_* = \left(\frac{g}{\theta_0} \langle w' \theta'_v \rangle |_{0z_{ML}} \right)^{1/3}, \quad (5)$$

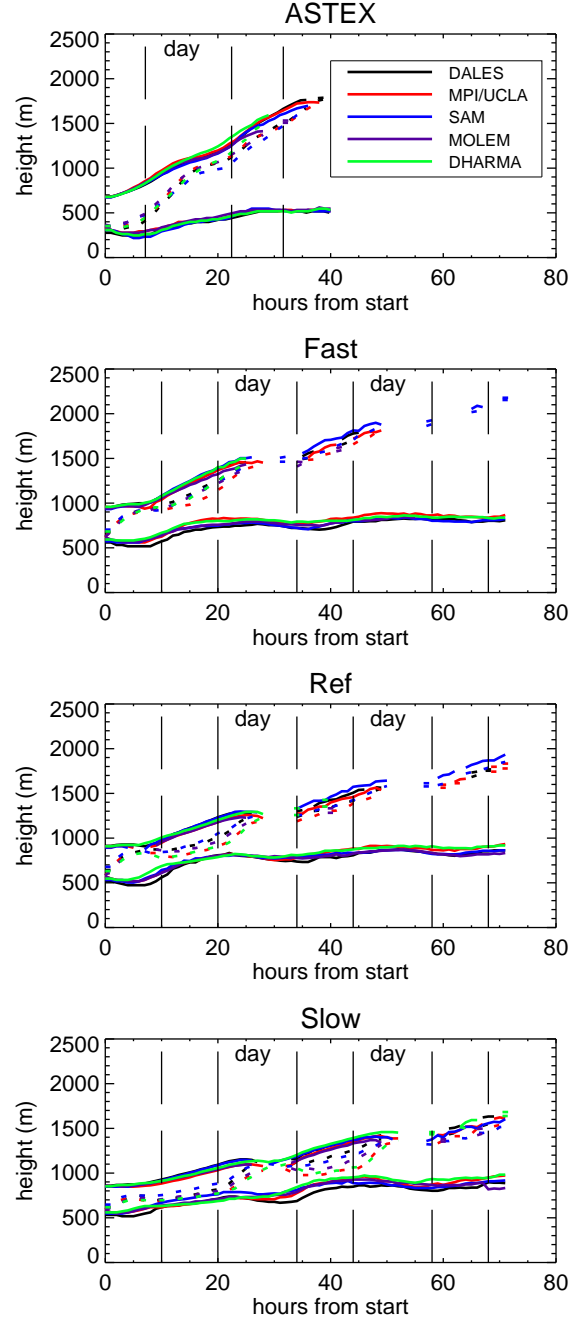


FIG. 3: The cloud boundaries for the ASTEX, Fast, Reference and Slow cases as a function of time. For each case and each model the lower solid line indicates the lowest cloud base height in the model. Above the cumulus cloud base, the dotted (solid) lines indicate the stratocumulus cloud base (top), which is defined as the lowest (highest) level where the cloud fraction exceeds 0.9. The line styles are according to the legend. The vertical dashed lines indicate the times of sunset and sunrise.

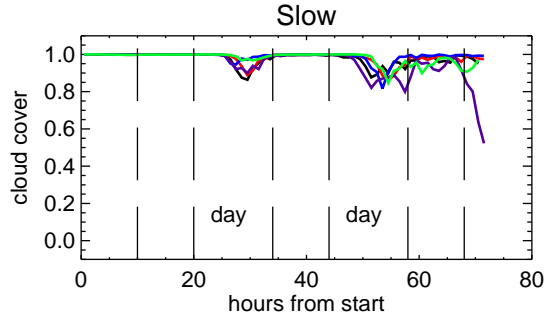
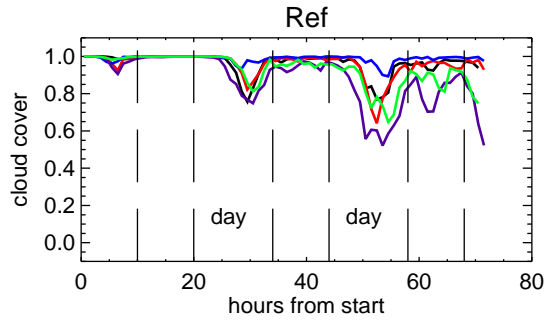
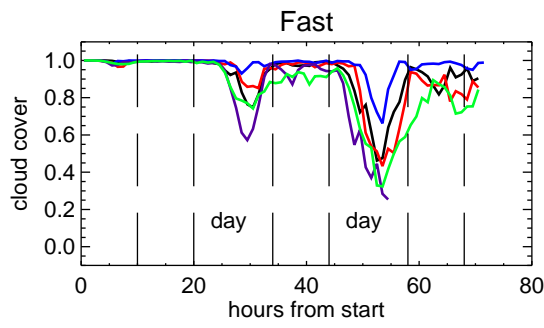
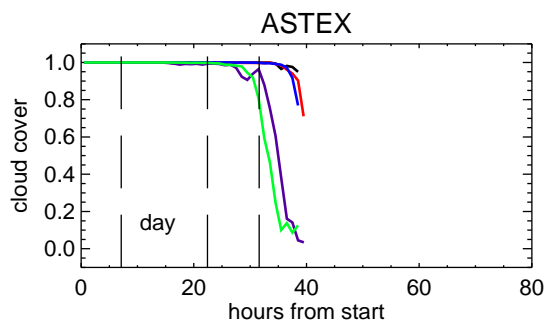


FIG. 4: The cloud cover for the ASTEX, Fast, Reference and Slow cases. Line styles as in Figure 3.

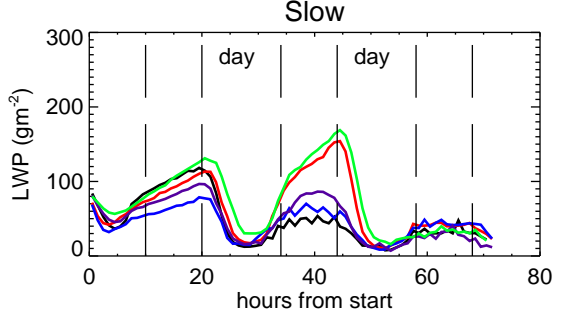
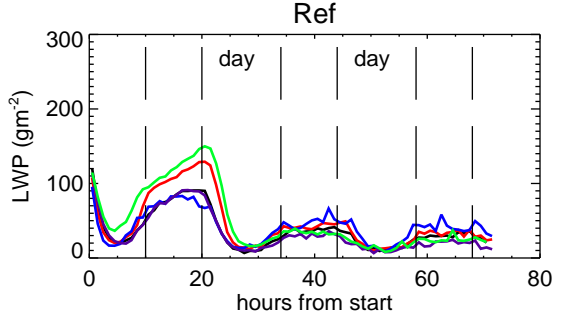
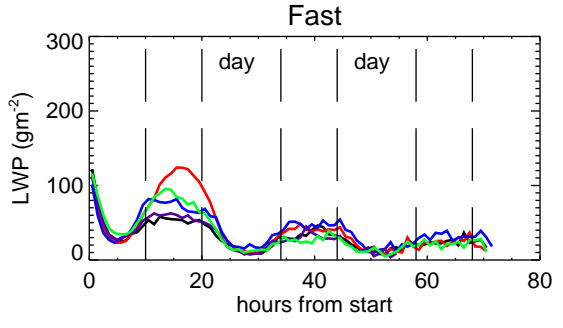
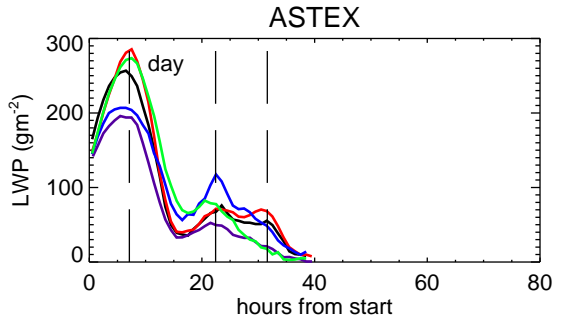


FIG. 5: The domain-averaged liquid water path for the ASTEX, Fast, Reference and Slow cases. Line styles as in Figure 3.

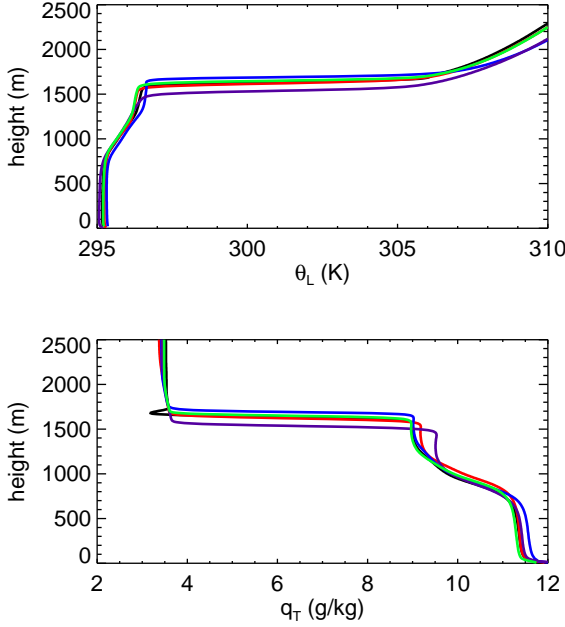


FIG. 6: Vertical profiles of the liquid water potential temperature and total specific humidity for the Reference case. The dashed lines represent a time-mean value during the 50th hour of the simulation. Line styles as in Figure 3.

where $\theta_0 = 300$ K is a reference temperature. For the last part of the ASTEX Lagrangian experiment this relation was found to represent the aircraft data rather well. Also LES results of the shallow cumulus clouds over land and marine cumulus penetrating stratocumulus above confirmed this scaling behavior, except perhaps at the top of the subcloud layer where latent heat release effects start to produce positive buoyancy fluxes (Brown et al., 2002; Stevens et al., 2001).

As a first step to scan the subcloud layer dynamics we computed the buoyancy flux ratio r_{θ_v} defined as the ratio of the buoyancy flux at the top of the subcloud layer to its surface value,

$$r_{\theta_v} = \frac{\langle w' \theta'_v \rangle|_{z_{ML}}}{\langle w' \theta'_v \rangle_0}. \quad (6)$$

Figure 8 shows that after some simulation time this factor becomes constant at about $r_{\theta_v} \approx -0.2$, indicative of a decoupled boundary layer and similar to the typical value found in the dry convective boundary layer.

The vertical profiles displayed in Figure 9 exhibit a clear scaling behavior. The virtual potential temperature fluxes all fall approximately along a straight line connecting the surface to the minimum flux value near the subcloud layer top. The vertical velocity variance profiles have a peak near $z/z_{ML} \approx 0.4$. However, their magnitude is a slightly smaller with respect to the similarity relation.

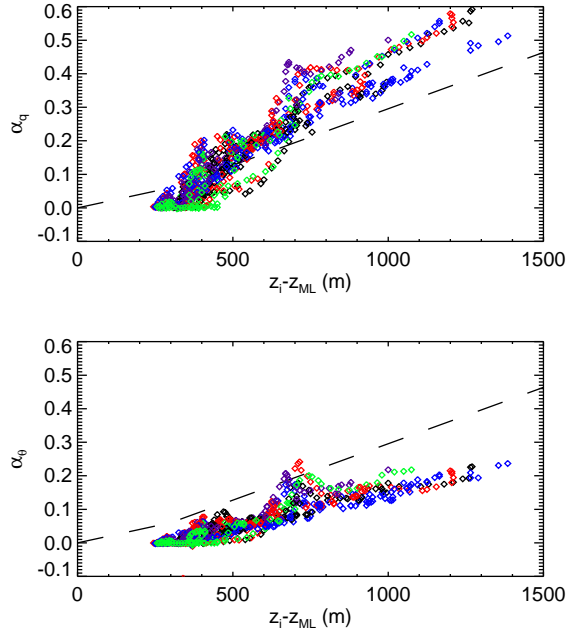


FIG. 7: Decoupling parameters α_q and α_θ . The dashed lines indicate a fit using the aircraft observations of α_q presented in Figure 5 of Wood and Bretherton (2004). The colors of the data points represent results from the different LES models and are chosen according to the color coding displayed in the legend of Figure 3.

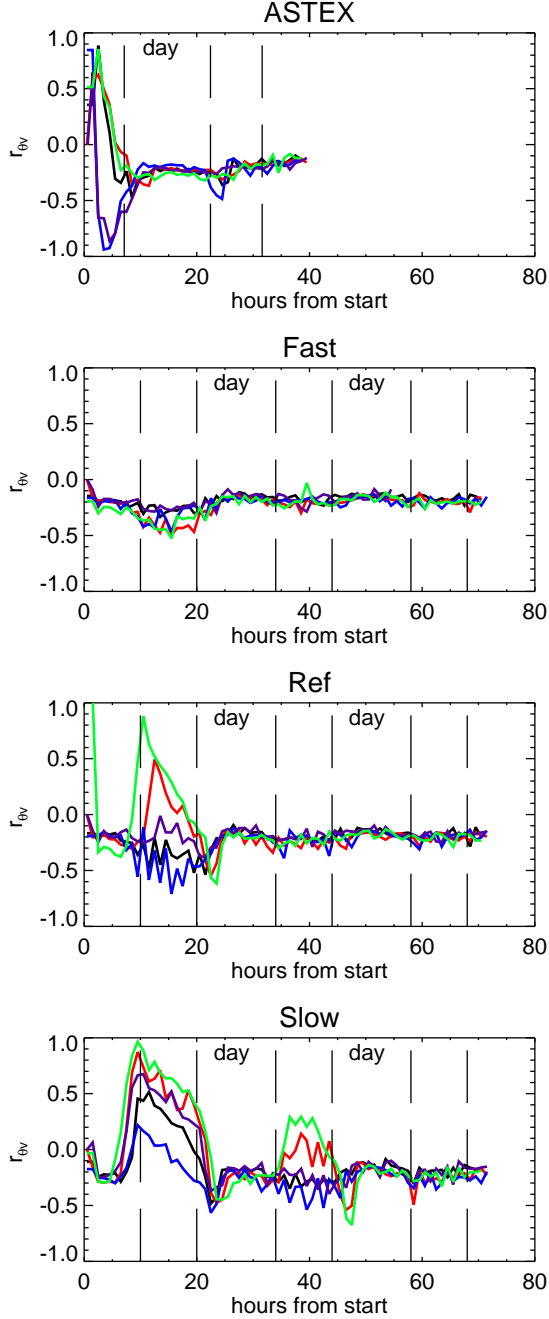


FIG. 8: The buoyancy flux ratio r_{θ_v} defined according to Eq. (6). Line styles as in Figure 3.

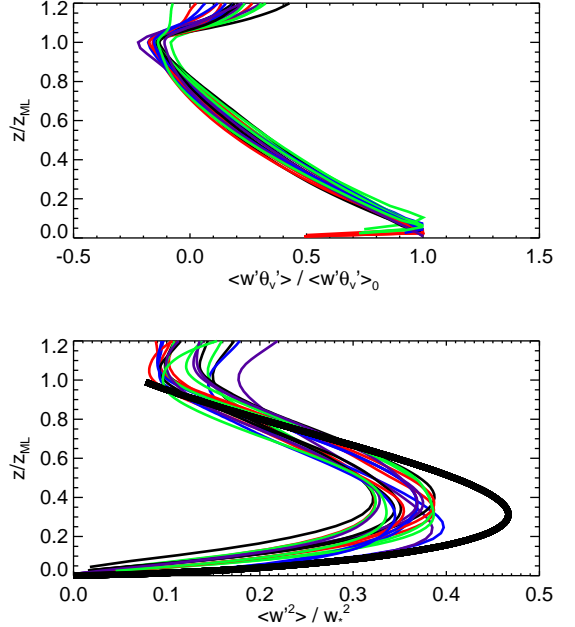


FIG. 9: The virtual potential temperature flux and the vertical velocity variance during daytime at $t=36$ h for ASTEX and $t=50$ h for the three composite cases. The thick black solid line represents the similarity relation for the vertical velocity variance in the dry convective boundary layer according to Eq (5). Line styles as in Figure 3.

5. BUDGETS OF HEAT AND MOISTURE IN THE BOUNDARY LAYER

Here we will briefly discuss the main components controlling the budgets of heat and moisture in the boundary layer. In particular, we will show the surface turbulent heat fluxes, entrainment rates, and precipitation at the cloud base. In addition we will discuss the moisture flux at the top of the subcloud layer, as this quantity determines the efficiency with which cumulus clouds can redistribute moisture from the subcloud layer to the stratocumulus at the top of the boundary layer.

Figure 10 shows the surface sensible and latent heat fluxes. The sensible heat fluxes are rather small, and after some time tend to obtain a constant value near 10 W/m^{-2} . The latent heat fluxes gradually increase with time, except for the ASTEX value. Typically the surface latent flux is proportional to a bulk drag coefficient and the surface gradient,

$$LE = \rho L_v C_d U_{ML} (q_{s,0} - q_{T,ML}), \quad (7)$$

where ρ is the density of air just above the sea surface, C_d a bulk drag coefficient, U_{ML} is the wind velocity in the subcloud mixed layer, and $q_{s,0}$ is the saturation specific humidity at the sea surface. For the ASTEX case the latent heat flux decreases as a result of a weakening geostrophic forcing yielding lower wind velocities. The composite cases exhibit a weak diurnal cycle in the latent heat flux, although their values generally tend to increase with time.

The entrainment rate w_e determines the fluxes of heat and moisture at the top of the boundary layer. According to the flux-jump relation the entrainment flux $w' \psi'_T$ of an arbitrary quantity ψ is given by

$$\overline{w' \psi'_T} = -w_e \Delta \overline{\psi}, \quad (8)$$

where $\Delta \overline{\psi}$ is the jump of ψ across an infinitesimally thin inversion layer. The entrainment rates are the largest for ASTEX and the Fast cases, with maximum values exceeding 1.5 cm/s during nighttime. The strength of the temperature inversion jump seems to be the first-order effect controlling the entrainment rate. During the night the entrainment rates are maximum, and during the day they diminish strongly as a result of absorption of shortwave radiation in the cloud layer. The day-time entrainment for the Slow and Reference case is less than 0.4 cm/s , which is similar to the first entrainment results obtained from aircraft observations in daytime stratocumulus cloud decks off the southern Californian coast by Kawa and Pearson (1989).

It is interesting to look at the moisture flux ratio r_{q_T} , which we define similar to the buoyancy flux ratio,

$$r_{q_T} = \frac{\langle w' q'_T \rangle|_{z_{ML}}}{\langle w' q'_T \rangle_0}. \quad (9)$$

If $r_{q_T} = 0$, all the moisture that is evaporated from the surface is trapped in the subcloud layer. On the other hand, if $r_{q_T} = 1$, the cumulus cloud remove moisture out

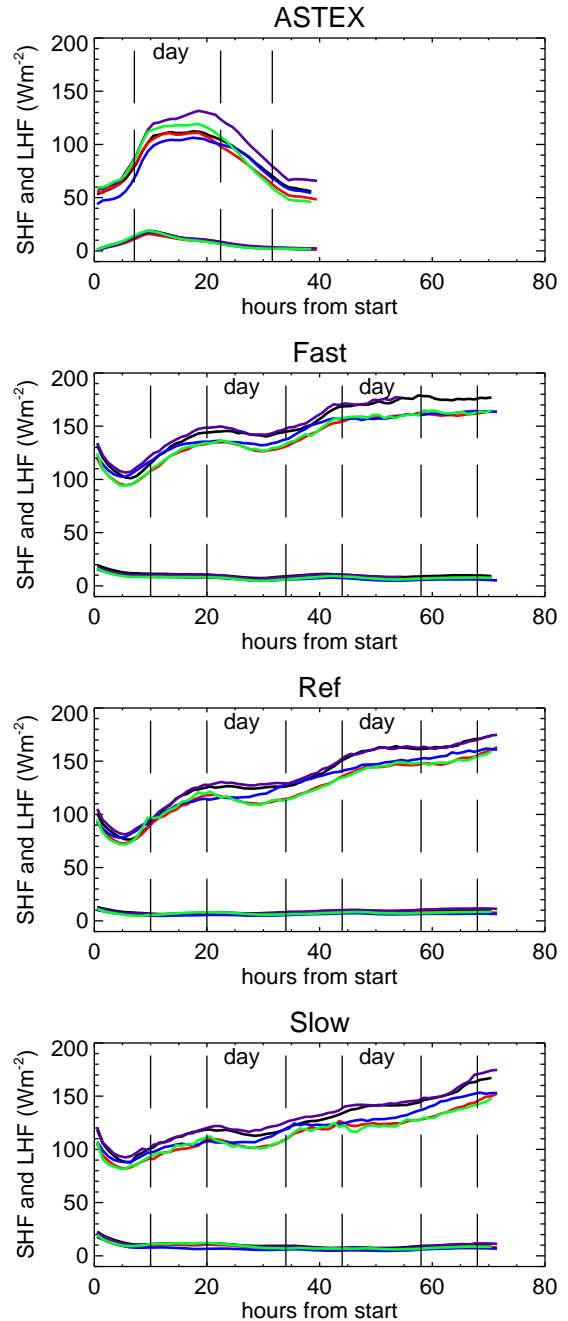


FIG. 10: The sensible and latent heat fluxes at the surface for the ASTEX, Fast, Reference and Slow cases. For all cases the sensible heat fluxes are in the group of low flux values with end values of about 10 W/m^{-2} . Line styles as in Figure 3

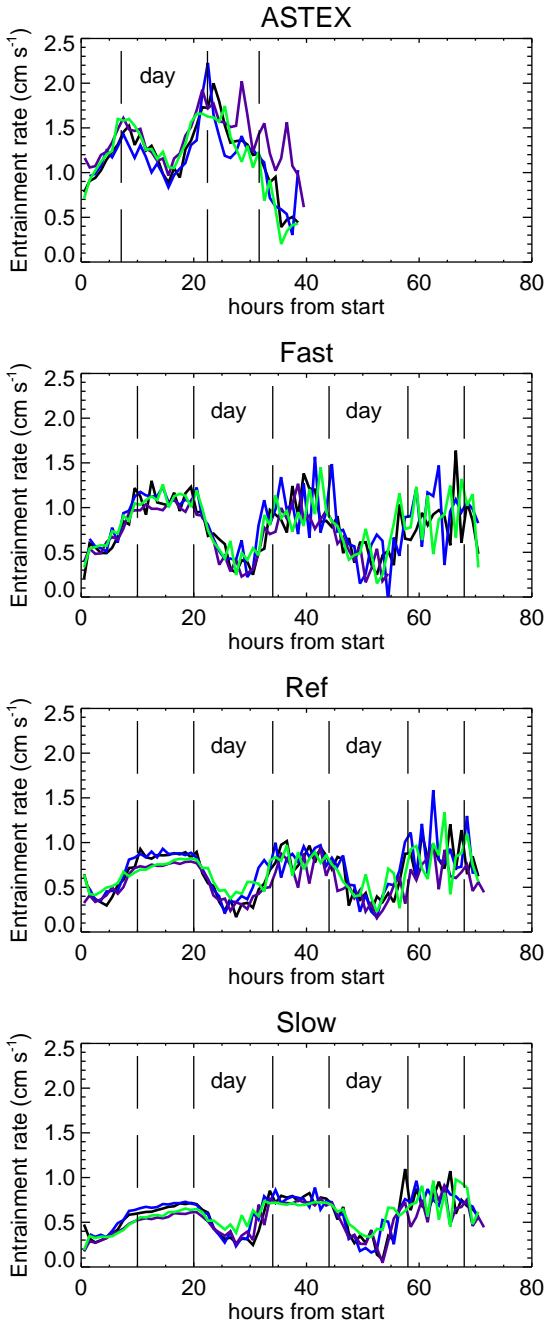


FIG. 11: The entrainment rate for the ASTEX, Fast, Reference and Slow cases. The used colors are the same as in Figure 3.

of the subcloud layer at the same rate as the evaporation. This limit, sometimes referred to as the zero-flux divergence assumption, has been used in the past in large-scale models as a parameterization for the moisture flux at the cumulus cloud base. Figure 12 shows a clear diurnal cycle in r_{qT} . During daytime moisture is trapped in the subcloud layer, but during the night the cumuli remove more moisture from the subcloud layer than is evaporated from the surface.

Last, we investigate the precipitation flux at the cloud base. Comstock et al. (2004) found the following relation from observations,

$$P_{cb} = 0.37 \left(\frac{LWP}{N_d} \right)^{1.75}, \quad (10)$$

with P_{cb} the cloud base precipitation flux at cloud base and N_d the cloud droplet concentration number. This relation is shown in Figure 12 for comparison with the LES results. The UCLA/MPI and DALES models give significantly lower precipitation rates at the cloud base than the parameterization.

6. ANALYSIS OF TIME SCALES IN THE SUBCLOUD LAYER

The fact that the virtual potential temperature flux becomes constant at the top of the subcloud layer can be used to obtain analytical solutions for the subcloud layer evolution. We will perform a similar analysis as Schubert et al. (1979). They solved the budget equations for a cloudy boundary layer that is well mixed from the surface to its top. In that case the heat and moisture budgets will be determined by turbulent fluxes at the surface, entrainment, precipitation and radiation. The LES results show that the stratocumulus-topped boundary layer rapidly becomes decoupled from the subcloud layer. However, the LES results give support for the notion that the subcloud layer is vertically well mixed. In the following we will consider the subcloud layer budgets of heat and moisture, using the fact that the system can be closed with aid of the buoyancy flux ratio r_{θ_v} .

We will consider a Lagrangian air mass that moves along with the mean flow. In that case there will be a negligibly small large-scale horizontal advection. Furthermore, because the subcloud layer is clear, we neglect radiation and precipitation. The latter assumption may be questionable in case of the presence of deep precipitating cumulus clouds above the subcloud layer. For the shallow boundary layer cloud convection studied here this is an acceptable assumption. Given this framework, the tendency for the virtual potential temperature in the subcloud layer is governed by the turbulent flux divergence,

$$\frac{\partial \theta_{v,ML}}{\partial t} = - \frac{\partial \langle w' \theta'_v \rangle}{\partial z} \quad (11)$$

where $\theta_{v,ML}$ is assumed to be constant with height. If we use the definition of the buoyancy flux ratio r_{θ_v} according to Eq. (6) the tendency equation becomes

$$\frac{\partial \theta_{v,ML}}{\partial t} = (1 - r_{\theta_v}) \frac{\langle w' \theta'_v \rangle_0}{z_{ML}}. \quad (12)$$

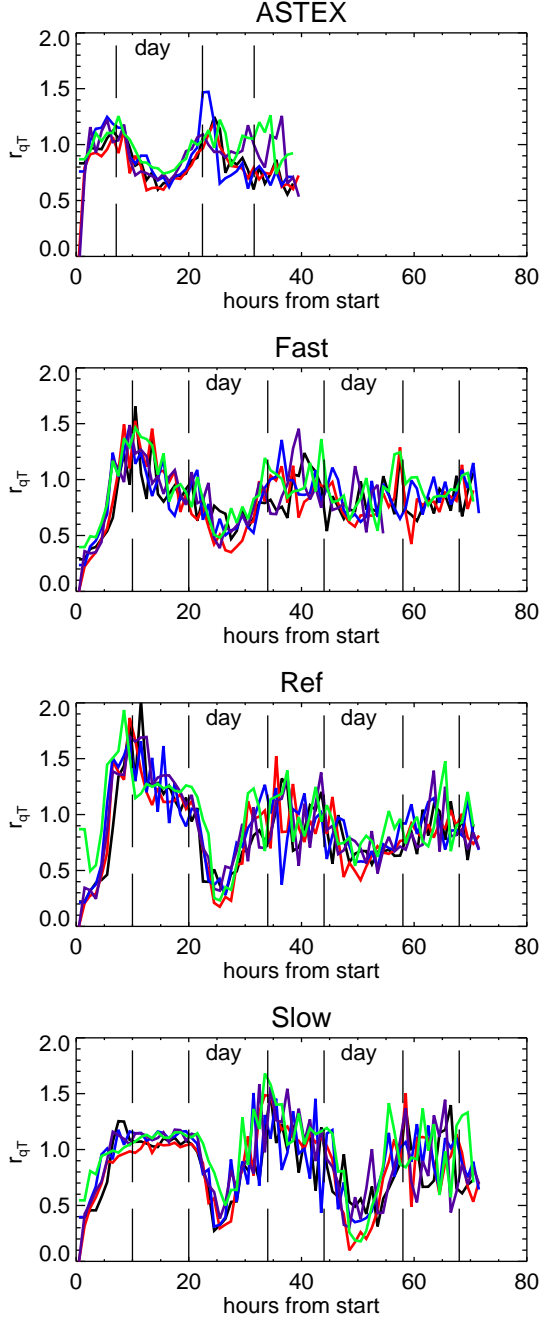


FIG. 12: The moisture flux ratio r_{qT} defined according to Eq. (9). Line styles as in Figure 3.

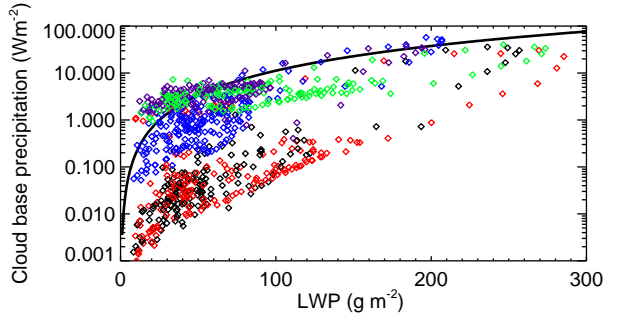


FIG. 13: The colors of the data points represent results from the different LES models and are chosen according to the color coding displayed in the legend of Figure 3.

To allow for an analytic solution, and on the basis of the results presented in Figure 3, it will be assumed that the cumulus subcloud layer height is constant with time.

This assumption may appear counterintuitive as the nonzero value for the buoyancy flux at the top of the subcloud layer suggests that air is entrained into the top of the subcloud layer. Such a process should cause a growth of the subcloud layer thickness. However, this growth can be opposed by shallow cumulus clouds that remove mass from the subcloud mixed layer. To this end we will apply a bulk formula for the surface flux of any arbitrary quantity ψ

$$\langle w' \psi' \rangle_0 = C_d U_{ML} (\psi_0 - \psi_{ML}), \quad (13)$$

to give

$$\begin{aligned} \frac{\partial \theta_{v,ML}}{\partial t} &= \left(\frac{1 - r_{\theta_v}}{z_{ML}} \right) C_d U_{ML} (\theta_{v,0} - \theta_{v,ML}) \\ &= \frac{\theta_{v,0} - \theta_{v,ML}}{\tau_{\theta}}, \end{aligned} \quad (14)$$

where the last step defines a time scale

$$\tau_{\theta} \equiv \frac{z_{ML}}{(1 - r_{\theta_v}) C_d U_{ML}}. \quad (15)$$

For $z_{ML} = 500$ m, $r_{\theta_v} = -0.2$, $C_d = 0.001$, $U_{ML} = 10$ m/s, we obtain $\tau_{\theta} = 11.6$ h.

Now we allow the surface virtual potential temperature $\theta_{v,0}$ to be time-dependent,

$$\theta_{v,0}(t) = \theta_{v,00} + U_{ML} \left(\frac{\partial \theta_{v,0}}{\partial x} \right) t = \theta_{v,00} + \gamma t, \quad (16)$$

with $\gamma \equiv \frac{\partial \theta_{v,0}}{\partial x}$ the horizontal gradient of the sea surface virtual potential temperature in the direction of the mean flow. For $U_{ML} = 10$ m/s, and if the sea surface virtual potential temperature changes by about 3 K/1000 km, then $\gamma = 0.11$ K/h. The budget equation now becomes

$$\frac{\partial \theta_{v,ML}}{\partial t} + \frac{\theta_{v,ML}}{\tau_{\theta}} = \frac{\theta_{v,00} + \gamma t}{\tau_{\theta}}, \quad (17)$$

which has the solution

$$\theta_{v,ML}(t) = \gamma t + C_1 + C_2 e^{-t/\tau_{\theta}}, \quad (18)$$

with $C_1 = \theta_{v,00} - \gamma\tau_\theta$ and $C_2 = \gamma\tau_\theta + \theta_{v,ML}(t=0) - \theta_{v,00}$. For $t \gg \tau_\theta$ the memory term, i.e. the last term which includes information about the initial state, vanishes. It is also clear that the tendency of $\theta_{v,ML}$ becomes similar to the sea surface. This has an important consequence for the surface buoyancy flux, which becomes clear for long time scales, i.e. $t \gg \tau_\theta$,

$$\theta_{v,0} - \theta_{v,ML} = \gamma\tau_\theta. \quad (19)$$

Thus according to the bulk surface flux equation (20) the surface buoyancy flux becomes constant with time,

$$\langle w'\theta'_v \rangle_0 = C_d U_{ML} \gamma \tau_\theta = \frac{\gamma z_{ML}}{1 - r_{\theta_v}}. \quad (20)$$

The equilibrium surface buoyancy flux value is thus proportional to the depth of the subcloud layer and to the horizontal gradient of the sea surface along the path of the air mass.

Likewise, we can write for the humidity in the mixed layer $q_{T,ML}$

$$\begin{aligned} \frac{\partial q_{T,ML}}{\partial t} &= \left(\frac{1 - r_{q_T}}{z_{ML}} \right) C_d U_{ML} (q_{s,0} - q_{T,ML}) \\ &= \frac{q_{s,0} - q_{T,ML}}{\tau_q}, \end{aligned} \quad (21)$$

where

$$\tau_q \equiv \frac{z_{ML}}{(1 - r_{q_T}) C_d U_{ML}}. \quad (22)$$

Note that if all the moisture that is evaporated from the surface is transported out of the mixed layer by cumulus clouds, a situation which in some NWPs has been assumed to generally hold for cumulus clouds over the ocean and referred to as the 'zero-flux divergence' assumption, gives $\tau_q = \infty$. This example illustrates that the time scales for moisture and heat differ in the subcloud layer.

The LES results indicate that the moisture flux ratio exhibits a clear diurnal cycle. In the following we will assume it is constant with time and its value can be loosely interpreted as a diurnal mean value. It will be shown that the time scales for the subcloud layer humidity are much larger than diurnal time scales. We consider the situation in which the sea surface temperature varies linearly with time according to

$$T_0(t) = T_{00} + \gamma t, \quad (23)$$

where T_{00} is the sea surface temperature at $t = 0$. By using γ , we assume that differences in the tendencies for the virtual potential temperature and temperature can be neglected. To take into account changes in the saturation specific humidity just above the surface we will use the Clausius-Clapeyron equation, which reads

$$\frac{\partial q_s}{\partial T} = \frac{L_v q_s}{R_v T^2}, \quad (24)$$

which can be approximated by (Stevens, 2006)

$$q_s(T) = q_{s,00} \exp \left[\frac{L_v}{R_v T_{00}^2} (T - T_{00}) \right] \quad (25)$$

where $q_{s,00} = q_s(T_{00})$. If the temperature increases linearly with time, then the saturation specific humidity at the surface will follow an exponential increase with time,

$$q_{s,0}(t) = q_{s,00} e^{t/\tau_c}, \quad (26)$$

where $\tau_c = \frac{R_v T_{00}^2}{L_v \gamma} = 131$ h. The differential equation to be solved then becomes

$$\frac{\partial q_{T,ML}}{\partial t} + \frac{q_{T,ML}}{\tau_q} = \frac{q_{s,00}}{\tau_q} e^{t/\tau_c}. \quad (27)$$

The solution reads

$$q_{T,ML}(t) = \frac{q_{s,00}}{1 + \frac{\tau_q}{\tau_c}} e^{t/\tau_c} + C_3 e^{-t/\tau_q}, \quad (28)$$

with

$$C_3 = q_{T,ML}(t=0) - \frac{q_{s,00}}{1 + \frac{\tau_q}{\tau_c}}. \quad (29)$$

We can immediately see that for a zero flux divergence assumption $r_{q_T} = 0$, the time scale $\tau_q = \infty$, and consequently the analytic solution gives a constant value with time for the mixed layer humidity, $q_{T,ML}(t) = q_{T,ML}(t=0)$.

The solution can be expressed as a function of the saturation specific humidity at the surface,

$$q_{T,ML}(t) = \frac{q_{s,0}(t)}{1 + \frac{\tau_q}{\tau_c}} + C_3 e^{-t/\tau_q}, \quad (30)$$

Because $\tau_q/\tau_c > 0$, it can thus be concluded that the specific humidity in the mixed layer increases at a lesser rate than the saturation value at the sea surface. The surface flux becomes

$$\langle w'q'_T \rangle_0 = C_d U_{ML} \left[\frac{\tau_q q_{s,00}}{\tau_c + \tau_q} e^{t/\tau_c} - C_3 e^{-t/\tau_q} \right]. \quad (31)$$

7. CONCLUSIONS

The LES models are capable of reproducing the stratocumulus to cumulus transition very consistently. They all show that the stratocumulus cloud layer gradually grows in time, and that the temporal variations in the shallow cumulus cloud base are rather small. The subcloud layer dynamics, in this case defined by the buoyancy flux and the vertical velocity variance, exhibit a similar scaling behavior as the clear convective boundary layer. The moisture flux in the subcloud layer shows a distinct diurnal cycle. During the day moisture gets trapped in the subcloud layer. However, during the night cumulus clouds are more actively redistributing the moisture out of the subcloud layer to the stratocumulus cloud layer. As a consequence a broken stratocumulus cloud deck can recover to a full cloud cover again.

The fact that the sea surface temperature increases along the Lagrangians causes a gradual increase in the surface evaporation. As a large fraction of the moisture is being transported to the stratocumulus, an enhancement of the surface evaporation tends to increase the lifetime of the stratocumulus. On the other hand, a warming sea surface decreases the bulk stability of the system,

as both the lower tropospheric stability and the difference in the humidity between the boundary layer and the free atmosphere increases.

ACKNOWLEDGMENTS

The investigations were done as part of the European Union Cloud Intercomparison, Process Study & Evaluation Project (EUCLIPSE) project, funded under Framework Program 7 of the European Union. We thank Dr. Chris Bretherton for providing an extensive set of input parameters for the ASTEX case. The simulations with the Dutch LES model were sponsored by the National Computing Facilities Foundation (NCF) for the use of supercomputer facilities.

REFERENCES

Albrecht, B. A., C. S. Bretherton, D. W. Johnson, W. H. Schubert, and A. S. Frisch, 1995: The Atlantic stratocumulus transition experiment - ASTEX. *Bull. Amer. Meteorol. Soc.*, **76**, 889–904.

Bretherton, C. S., P. Austin, and S. T. Siems, 1995: Cloudiness and marine boundary layer dynamics in the ASTEX Lagrangian experiments. Part II: Cloudiness, drizzle, surface fluxes and entrainment. *J. Atmos. Sci.*, **52**, 2724–2735.

Bretherton, C. S., S. K. Krueger, M. C. Wyant, P. Bechtold, E. V. Meijgaard, B. Stevens, and J. Teixeira, 1999: A GCSS boundary-layer cloud model intercomparison study of the first ASTEX Lagrangian experiment. *Boundary-Layer Meteorol.*, **93**, 341–380.

Bretherton, C. S. and R. Pincus, 1995: Cloudiness and marine boundary layer dynamics in the ASTEX Lagrangian experiment. Part I: synoptic setting and vertical structure. *J. Atmos. Sci.*, **52**, 2707–2723.

Brown, A. R., et al., 2002: Large-eddy simulation of the diurnal cycle of shallow cumulus convection over land. *Quart. J. Roy. Meteorol. Soc.*, **128**, 1075–1093.

Comstock, K. K., R. Wood, S. E. Yuter, and C. S. Bretherton, 2004: Reflectivity and rain rate in and below drizzling stratocumulus. *Quart. J. Roy. Meteorol. Soc.*, **130**, 2891–2918.

De Roode, S. R. and P. G. Duynkerke, 1997: Observed Lagrangian transition of stratocumulus into cumulus during ASTEX: Mean state and turbulence structure. *J. Atmos. Sci.*, **54**, 2157–2173.

Heus, T., et al., 2010: Formulation of the dutch atmospheric large-eddy simulation (DALES) and overview of its applications. *Geosci. Model Development*, **3**, 415–444, doi:doi:10.5194/gmd-3-415-2010.

Kawa, S. R. and R. Pearson, 1989: An observational study of stratocumulus entrainment and thermodynamics. *J. Atmos. Sci.*, **46**, 2650–2661.

Khairoutdinov, M. K. and D. A. Randall, 2005: Cloud-resolving modeling of the ARM summer 1997 IOP: Model formulation, results, uncertainties and sensitivities. *J. Atmos. Sci.*, **60**, 607–625.

Lenschow, D. H., J. C. Wyngaard, and W. T. Pennell, 1980: Mean field and second-moment budgets in a baroclinic, convective boundary layer. *J. Atmos. Sci.*, **37**, 1313–1326.

Lock, A. P., 2009: Factors influencing cloud area at the capping inversion for shallow cumulus clouds. *Quart. J. Roy. Meteorol. Soc.*, **135**, 941–952.

Neggers, R. A. J., B. Stevens, and J. D. Neelin, 2006: A simple equilibrium model for shallow-cumulus topped mixed layers. *Theor. Comput. Fluid Dyn.*, **20**, 305–322.

Park, S., C. B. Leovy, and M. A. Rozendaal, 2004: A new heuristic lagrangian marine boundary layer cloud model. *J. Atmos. Sci.*, **61**, 3002–3024.

Sandu, I. and B. Stevens, 2011: On the factors modulating the stratocumulus to cumulus transitions. *J. Atmos. Sci.*, **68**, 1865–1881.

Sandu, I., B. Stevens, and R. Pincus, 2010: On the transitions in marine boundary layer cloudiness. *Atmos. Chem. Phys.*, **10**, 2377–2391.

Schubert, W. H., J. S. Wakefield, E. J. Steiner, and S. K. Cox, 1979: Marine stratocumulus convection. Part II: Horizontally inhomogeneous solutions. *J. Atmos. Sci.*, **36**, 1308–1324.

Stevens, B., 2006: Bulk boundary-layer concepts for simplified models of tropical dynamics. *Theor. Comput. Fluid. Dyn.*, doi:DOI10.1007/s00162-006-0032-z.

Stevens, B., et al., 2001: Simulations of trade wind cumuli under a strong inversion. *J. Atmos. Sci.*, **58**, 1870–1891.

Stevens, B., et al., 2005: Evaluation of large-eddy simulations via observations of nocturnal marine stratocumulus. *Mon. Weather Rev.*, **133**, 1443–1462.

Stevens, D. E., A. S. Ackerman, and C. S. Bretherton, 2002: Effect of domain size and numerical resolution on the simulation of shallow cumulus convection. *J. Atmos. Sci.*, **59**, 3285–3301.

Wood, R. and C. S. Bretherton, 2004: Boundary layer depth, entrainment, and decoupling in the cloud-capped subtropical and tropical marine boundary layer. *J. Climate*, **17**, 3576–3588.